

Frequency-dependent and algebraic bath states for a Dynamical Mean-Field Theory with compact support

Max Nusspickel¹ and George H. Booth^{1, a)}

Department of Physics, King's College London, Strand, London, WC2R 2LS, U.K.

(Dated: 18 September 2019)

We demonstrate an algebraic construction of frequency-dependent bath orbitals which can be used in a robust and rigorously self-consistent DMFT-like embedding method, here called ω -DMFT, suitable for use with Hamiltonian-based impurity solvers. These bath orbitals are designed to exactly reproduce the hybridization of the impurity to its environment, while allowing for a systematic expansion of this bath space as impurity interactions couple frequency points. In this way, the difficult non-linear fit of bath parameters necessary for many Hamiltonian-formulation impurity solvers in DMFT is avoided, while the introduction of frequency dependence in this bath space is shown to allow for more compact bath sizes. This has significant potential use with a number of new, emerging Hamiltonian solvers which allow for the embedding of large impurity spaces within a DMFT framework. We present results of the ω -DMFT approach for the Hubbard model on the Bethe lattice, a 1D chain, and the 2D square lattice, which show excellent agreement with standard DMFT results, with fewer bath orbitals and more compact support for the hybridization representation in the key impurity model of the method.

I. INTRODUCTION

Strongly correlated electron systems exhibit some of the most interesting macroscopic manifestations of quantum collective behavior, and as such have been of major interest both in the condensed matter physics and quantum chemistry community¹. Often these correlation effects manifest from strong interactions of electrons within local atomic-like degrees of freedom which lie close to the Fermi energy. Describing the strong interactions within these local ‘impurity’ orbitals while simultaneously describing their delocalized character into the wider system with which they are hybridized, is the driving principle of many quantum embedding methods. The dynamical mean-field theory (DMFT) has been successful in this regard, initially applied to the Hubbard model on an infinitely coordinated lattice, where its approximation of a strictly local self-energy is formally exact²⁻⁴. The core of the DMFT framework involves an impurity solver, where the dynamics of the interacting impurity is computed in the presence of some representation of its coupling to its environment via the hybridization function. A common approach is to rely on continuous-time quantum Monte-Carlo (CT-QMC) techniques, which allow for an integration over the entire action of this hybridization in a stochastic technique.⁵ Alternatively, there exists a growing body of research focussing on approaches to solve the impurity problem which exists within a Hamiltonian formulation. In order to do this, the hybridization must be discretized as a finite set of bath orbitals which are explicitly coupled to the impurity space. Traditionally, this resulting problem was solved with exact diagonalization (ED) methods (known as full configuration-interaction in the quantum chemistry community).

This has some advantages over CT-QMC, including the ability to solve the problem at strictly zero electronic temperature, the ability to compute real-frequency dynamical quan-

ties without relying on analytic continuation, the absence of stochastic errors, and the ability to seamlessly deal with arbitrary forms of the two-body impurity interactions. However, the price to pay is the discretization of the hybridization in terms of these bath orbitals, and the exponential cost of the solver as the number of bath orbitals is increased, necessitating a very compact number of orbitals to represent this continuous function.

This places severe limitations onto cluster DMFT methods, since one has to compromise between the description of long-range correlation by enlarging the impurity size and a faithful representation of the hybridization by including more bath orbitals, which can often limit the true physics of the system from emerging. To mitigate this, a number of lower cost Hamiltonian-formulation solvers are now being developed, which allow for a larger number of bath orbitals to be included, while admitting minimal error into the description of the impurity dynamics. These are based on selected configuration interaction, density matrix renormalization group, stochastic methods, and quantum chemical methodologies among others⁶⁻¹⁹. However, while these approaches can allow more bath orbitals, the difficulty in finding an appropriate and compact bath space, especially in situations where there are a larger number of impurities or a complex hybridization with substantial non-diagonal contributions, remains significant. This is due to the non-convex numerical optimization which is required, which can frequently result in local minima when constrained to a small number of bath orbitals, and whose many solutions when matching on the Matsubara axis can make a consistent level of description hard to achieve via this approach.

In this work we circumvent these problems via an algebraic approach to generate a compact set of explicit bath orbitals which define an impurity auxiliary system with well-defined properties, exactly capturing the hybridization and ensuring a rapid and systematic convergence of the bath space compared to traditional ED-DMFT. In addition, the approach avoids the non-linear numerical fit of bath orbitals of the impurity problem. The price we pay for these desirable properties is that the

^{a)}Electronic mail: george.booth@kcl.ac.uk

constructed bath space changes with frequency and therefore an impurity model has to be solved for each frequency point of interest. However, this property of the method rationalizes the claim of being able to capture the exact hybridization despite a finite bath space, as well as the prospect of a more compact bath space at each frequency point and reduction in the bath discretization error. The method is also exact in the non-interacting limit, with the cluster and lattice Green's function identical by construction due to the exact hybridization of the bath space. Due to the frequency-dependence of the auxiliary impurity problems, we term this approach ω -DMFT.

The method bears relation to a number of approaches in the literature that is worth expanding upon. The density-matrix embedding theory (DMET) takes a different approach to the embedding problem, which has also had a number of notable successes.^{20–22} In this method, the impurity problem has to be solved for the one-particle reduced density matrix only, reducing the computational cost greatly in comparison to DMFT. The coupling to the environment in order to reproduce the projection of this lattice density matrix is also algebraic and compact, further reducing the cost. This is obtained from the Schmidt decomposition of a mean-field wavefunction, ensuring an exact matching of the uncorrelated density-matrix between impurity model and lattice. However, the absence of dynamical effects restricts the local physics which can be described in DMET compared to DMFT. For instance, the lack of a self-consistent and dynamical self-energy in the lattice precludes the description of correlated physics such as local fluctuating moments, e.g. Mott insulating phases in the lattice, which are instead mimicked via symmetry-breaking. In order to describe dynamical correlation functions, it was shown in Ref. 23 that the DMET procedure could be augmented with a single-shot, non-self-consistent calculation of the Green's function, using bath orbitals derived from a Schmidt decomposition of a mean-field response function. However, the lack of dynamical effects in the lattice again precluded a self-consistent treatment.

In order to ameliorate these limitations of DMET, recently the 'energy-weighted density-matrix embedding theory' (EwDMET) was proposed as a way to add a controllable resolution of dynamical fluctuations between the impurity and environment, while still retaining a computationally efficient, static formulation.^{24,25} In this approach local energy-weighted density matrices are matched between the impurity and lattice, providing a limited, yet systematically improvable dynamical resolution of the impurity propagator. Furthermore, correlation effects in the lattice are self-consistently described by an effective dynamical self-energy, represented via additional auxiliary degrees of freedom on the lattice. True correlation-driven Mott physics was therefore demonstrated in a DMET context, even for a single impurity-site, without the necessity of symmetry-breaking.

The ω -DMFT approach detailed in this work can be considered an extension of the EwDMET method for spectral embedding, allowing for full dynamical effects of the impurity, and building on and generalizing the previous work of the construction of (non-self-consistent) bath spaces for spectral DMET^{23,26}. The systematic expansion in static bath orbitals

of EwDMET is generalized for a systematic expansion of explicitly *dynamic* bath orbitals to converge the bath discretization error for fully dynamical properties. As with EwDMET, this again relies on the representation of the self-consistently obtained self-energy in an explicit auxiliary-space representation, such that the Weiss field can also be represented via diagonalization of a quadratic Hamiltonian form²⁷. This allows for the use of Schmidt decomposition techniques on a single-particle wavefunction to derive appropriate bath orbitals suitable for a DMFT-like framework with explicit and fully dynamical effects (in comparison to the limited dynamical resolution of EwDMET). It may be argued that the construction of this auxiliary space representation of the self-energy is as challenging as the construction of the bath space in ED-DMFT. However in practice, this is a far less severe constraint than the original bath orbital problem required to represent the hybridization, as the cost of inclusion of additional auxiliary self-energy states is just (static) mean-field cost, and so the self-energy does not require a compact representation in terms of these auxiliary states.

In this work, we will test the ω -DMFT method on different lattices with the Hubbard Hamiltonian

$$H = h + H_U = -t \sum_{\langle ij \rangle, \sigma} c_{i\sigma}^\dagger c_{j\sigma} + U \sum_i n_i^\uparrow n_i^\downarrow, \quad (1)$$

where t describes the nearest neighbor hopping and U the on-site electron interaction. Despite its simplicity, the Hubbard Hamiltonian captures the competing effects of delocalization due to the kinetic energy term and localization due to the electron correlation. Additionally, for special lattice geometries, like the infinite dimensional and one-dimensional cases, exact solutions of some properties are known, which we will extensively compare against. Throughout this paper all energies are understood in units of t .

II. THEORY

We first give a short description of DMFT, while we refer to Refs. 4 and 28 for more in-depth reviews. We then present in more detail the individual steps of the ω -DMFT method, as well as the self-consistent algorithm and the calculation of total energy and spectral function.

A. DMFT

The fundamental approximation of DMFT is the neglect of non-local, long-range contributions to the electronic self-energy. Dividing a system of N_{sites} into $N_{\text{sites}}/N_{\text{imp}}$ fragments of size N_{imp} , which are related by some symmetry operation of the system, all blocks of the self-energy coupling different fragments are assumed zero by virtue of the DMFT approximation. In lattices with translational symmetry, this can be expressed as momentum-independence of the self-energy as $\Sigma(k, z) = \Sigma_{\text{imp}}(z)$, where $\Sigma(k, z)$ is the lattice self-energy of momentum k at frequency z and Σ_{imp} is the impurity self-energy. To calculate the latter, an impurity problem has to be

set up consisting of a single fragment coupled to its environment as given by the hybridization, which defines the single-particle character of this coupling. In the Hamiltonian formulation of this problem, this coupling is approximated by a set of N_b bath orbitals, which describe the effect of the frequency-dependent hybridization $\Delta(z)$ with the environment. The energies ε_p and couplings Γ_p (a vector) of each bath orbital describe the cluster hybridization

$$\Delta_c(z) = \sum_p \frac{\Gamma_p \otimes \Gamma_p^*}{z - \varepsilon_p}. \quad (2)$$

Finding appropriate bath parameters ε_p and Γ_p is one of the major challenges of ED-DMFT. In general, the process of finding an approximate $\Delta_c(z)$ for a given $\Delta(z)$ can be seen as a projection onto a functional subspace of all possible hybridizations.⁴ To perform this projection, one can introduce a distance function in the functional space and then numerically minimize this distance by varying all bath parameters. If performed on the imaginary frequency axis, the minimization is generally well behaved, for example using the distance function

$$d = \sum_n \frac{1}{\omega_n^M} \text{tr} |\Delta(i\omega_n) - \Delta_c(i\omega_n)|^2, \quad (3)$$

where N_ω determines a frequency cutoff and M a frequency weighting, which is often chosen between 0 and 2 (in this work we always use all available Matsubara points and $M = 1$). Instead of taking the difference of the hybridizations in Eq. (3), it is also possible to use the corresponding Green's functions instead.²⁹ The different ways of defining the distance function as well as an often significant dependence on the starting guess for the fit parameters, makes the fitting procedure an unsatisfying step of DMFT, which often needs to be tuned to the physical problem at hand. We note that alternative ways to obtain bath parameters exist, for example via a real-frequency description of the hybridization required for numerical renormalization group solvers^{30,31}, truncation of a continued-fraction representation³², or further constraints on the numerical fitting to improve the numerics.³³ Once the bath parameters are determined, the cluster Hamiltonian

$$H_c = \sum_{ab \in \text{imp}} h_{ab} c_a^\dagger c_b + U \sum_{a \in \text{imp}} n_a^\uparrow n_a^\downarrow + \sum_{p \in \text{bath}} \varepsilon_p c_p^\dagger c_p + \sum_{a \in \text{imp}} \sum_{p \in \text{bath}} (\Gamma_{ap} c_a^\dagger c_p + \text{h.c.}) \quad (4)$$

can be solved for the ground-state $|0\rangle$ and its energy E_0 via exact diagonalization. Note that we suppress spin indices and summations for simplicity, except for the interaction term where they are denoted explicitly. The impurity Green's function

$$G_{\text{imp},ab}(i\omega_n) = \langle 0 | c_a [i\omega_n - (H_c - E_0)]^{-1} c_b^\dagger | 0 \rangle \quad (5)$$

$$+ \langle 0 | c_b^\dagger [i\omega_n + (H_c - E_0)]^{-1} c_a | 0 \rangle \quad (6)$$

can be calculated via a number of different methods, traditionally the dynamical Lanczos approach³⁴. However in this

work, we use a more accurate approach which computes the Green's function exactly, one frequency at a time, via the correction vector method^{35,36}. The impurity self-energy is then defined by the Dyson equation

$$\Sigma_{\text{imp}}(i\omega_n) = i\omega_n - h_{\text{imp}} - \Delta_c(i\omega_n) - G_{\text{imp}}^{-1}(i\omega_n), \quad (7)$$

where h_{imp} is the projection of the one-electron Hamiltonian into the impurity space. The impurity self-energy can be unfolded into the lattice self-energy using the symmetry operations of the underlying system. Labelling the equivalent fragments with R and R' , this can be written as

$$\Sigma_{RR'}(i\omega_n) = \delta_{RR'} \Sigma_{\text{imp}}(i\omega_n). \quad (8)$$

The lattice self-energy defines the lattice Green's function $G(i\omega_n) = [i\omega_n - h - \Sigma(i\omega_n)]^{-1}$, which in turn defines a new hybridization function

$$\Delta(i\omega_n) = i\omega_n - h_{\text{imp}} - [G_{00}(i\omega_n)]^{-1} - \Sigma_{00}(i\omega_n), \quad (9)$$

where G_{00} and Σ_{00} refer to the impurity part of the lattice Green's function and self-energy, respectively. From the new hybridization, an updated set of bath parameters ε and Γ can be fitted via the minimization of Eq. (3). This procedure is then iterated until self-consistency is achieved.

An advantage of the ED solver in DMFT is that the ill-conditioned analytic continuation from Matsubara Green's function to the real axis is circumvented. Instead, once the bath parameters are converged on the Matsubara axis, the impurity Green's function can be calculated at real frequencies. As a consequence of the bath discretization error, the spectral function obtained this way will in general not be smooth, as it will necessarily be represented as a sum of a finite number of individual poles of the impurity model. Alternatively, one can calculate the self-energy on the real-frequency axis, and then subsequently compute the spectral function in the lattice space, according to

$$A(\omega) = -\frac{1}{\pi} \text{Im} G_{00}^R(\omega) [\Sigma(\omega)], \quad (10)$$

where G^R is the retarded Green's function of the lattice. This will remove the explicit bath discretization error in the one-particle Hamiltonian and therefore yield smoother spectra, however it will still potentially suffer from the implicit error due to the bath discretization effects in the self-energy. With the exception of Fig. 1, the DMFT spectral functions shown in this paper are calculated according to Eq. (10).

B. ω -DMFT

Since a compact and robust bath parameterization via numerical minimization of Eq. (3) is a major difficulty in DMFT calculations, we avoid it by constructing bath orbitals algebraically from an expression that is derived from the Schmidt decomposition of a mean-field response wavefunction, given by

$$|\phi_a^{(1)}(z)\rangle = \frac{1}{z - h} c_a^{(\dagger)} |\Phi_0\rangle, \quad (11)$$

where h is a quadratic Hamiltonian which can implicitly include the effects of a self-consistent self-energy, thereby generalizing the work of Ref. 23. The bath orbitals will thus inherit the frequency-dependence of the response wavefunction, ultimately resulting in a different cluster problem for each frequency. In contrast to standard DMFT, ω -DMFT will guarantee that the uncorrelated Green's function is exactly reproduced in the impurity space (i.e. in the absence of explicit two-electron terms). As a consequence of the Dyson equation, the hybridization is therefore also exactly matched. The Schmidt decomposition technique comes with the caveat that only single Slater-determinant wavefunctions can be decomposed into one-electron bath orbitals. Therefore, as an additional difference to standard DMFT, it is thus necessary to augment the system with auxiliary degrees of freedoms, which describe the effect of the dynamical self-energy on the lattice, whilst ensuring that h in Eq. 11 remains a quadratic Hamiltonian.

In the following subsections we describe the derivation of the bath orbitals as well as the other steps of the ω -DMFT method in more detail.

1. Bath construction

The wavefunctions which we aim to Schmidt decompose in order to find the appropriate bath states can be written in their most general form as $f(H)c_a^{(\dagger)}|0\rangle$ where f is a function of the Hamiltonian H . In this work we restrict ourselves to a Hamiltonian which is quadratic in the electron-field, so that its true ground-state $|0\rangle$ can be expressed as a single Slater-determinant $|\Phi_0\rangle$. The bath wavefunctions then become simple tensor products of single bath orbitals and a determinant of the remaining orbitals in $|\Phi_0\rangle$ ³⁷. Many-body effects via an implicit self-energy can still be retained via an augmented one-electron Hamiltonian h_{Weiss} , which we will define in Sec. II B 2. In the first iteration (i.e. in the absence of an effective self-energy), $h_{\text{Weiss}} = h$.

In EwDMET, the decomposition is done on the wavefunction $(h_{\text{Weiss}})^m c_a^{(\dagger)}|\Phi_0\rangle$, which leads to the particle and hole bath orbitals

$$|b_{a,m}^>\rangle = \sum_{x \notin \text{imp}} \sum_{i: \varepsilon_i > \mu} C_{ai} \varepsilon_i^m C_{xi} |x\rangle \quad m \geq 0 \quad (12)$$

$$|b_{a,m}^<\rangle = \sum_{x \notin \text{imp}} \sum_{i: \varepsilon_i < \mu} C_{ai} \varepsilon_i^m C_{xi} |x\rangle \quad m > 0, \quad (13)$$

where C and ε are the eigenvectors and eigenvalues of h_{Weiss} .²⁴ We will call these orbitals *static* bath orbitals to distinguish them from the frequency-dependent dynamic bath orbitals, which will be introduced below. The standard DMET bath orbitals are the special case $m = 0$ of these orbitals. Note that in this $m = 0$ case the particle and hole orbitals are linearly dependent and the hole orbitals can thus be restricted to orders greater than zero. The particle static bath orbitals ensure that the moments of the particle (unoccupied) spectral function, $T_{ab,n}^> = \sum_{i: \varepsilon_i > \mu} C_{ai} \varepsilon_i^n C_{bi}$, are matched between h_{Weiss} and its projection into the impurity+bath space, and similarly

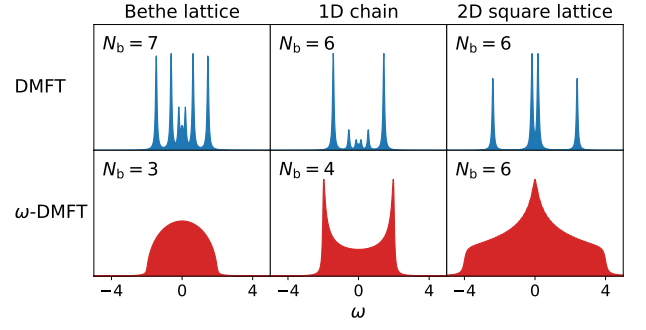


FIG. 1. Impurity Green's function of the auxiliary model for DMFT and the ω -DMFT method for different lattice geometries in the absence of explicit two-body impurity interactions. The introduction of frequency-dependent bath orbitals in ω -DMFT means that the impurity Green's function in the auxiliary system exactly matches the desired lattice spectrum, resulting in an exact hybridization and smooth spectral functions, despite a small finite bath space of N_b orbitals.

for the hole (occupied) bath orbitals. The maximum moment n that will be exactly matched by including all bath orbitals up to order M_s is given by $n = 2M_s + 1$, where M_s denotes the maximum exponent m in Eqs. 12 and 13.²⁴ Since the moments relate directly to the high frequency expansion of the Green's function $(z - h_{\text{Weiss}})^{-1}$, adding static bath orbitals corresponding to higher moments can be seen as a systematic expansion of the Green's function in the high-frequency limit, though the fact that particle and hole moments are separately matched means that this is not purely a high-energy expansion.

In order to match the Green's function between lattice and cluster space, we apply the Schmidt decomposition directly to frequency-dependent wavefunction $(z - h_{\text{Weiss}})^{-1} c_a^{(\dagger)}|\Phi_0\rangle$, which was proposed in Ref. 23. The advantage of using frequency-dependent bath orbitals constructed this way is exemplified in Fig. 1, where the impurity density of states (DoS) of the auxiliary impurity+bath system is compared between standard DMFT and ω -DMFT at $U = 0$. While the bath discretization is very apparent in the DMFT case, the dynamic bath orbitals of ω -DMFT guarantee that the uncorrelated Green's function is exact at every frequency, even in the presence of an effective self-energy in the lattice.

To additionally match frequency-derivatives of the Green's function at z , we can generalize the construction above and decompose $(z - h_{\text{Weiss}})^{-m} c_a^{(\dagger)}|\Phi_0\rangle$ instead, with $m = 1$ representing the previous case. The Schmidt decomposition of this wavefunction results in the dynamic bath orbitals

$$|f_{a,m}^>(z)\rangle = \sum_{x \notin \text{imp}} \sum_{i: \varepsilon_i > \mu} \frac{C_{ai} C_{xi}}{(z - \varepsilon_i)^m} |x\rangle \quad m > 0 \quad (14)$$

$$|f_{a,m}^<(z)\rangle = \sum_{x \notin \text{imp}} \sum_{i: \varepsilon_i < \mu} \frac{C_{ai} C_{xi}}{(z - \varepsilon_i)^m} |x\rangle \quad m > 0. \quad (15)$$

One might expect that every order of dynamic bath orbitals matches two orders of derivatives of the Green's function, similar how every static bath order ensures the matching of

two additional moments. However, this is only the case if also the complex conjugated counterparts to Eqs. (14,15) are added to the bath space. This would then result in the rule $n = 2M_d - 1$, where n is the maximum derivative that is matched (with $n = 0$ referring to the value of the hybridization at frequency z) and M_d is the maximum order m for which the dynamic bath orbitals and their complex conjugates are included. Equivalently one can add the real and imaginary part of the dynamic bath orbitals individually, spanning the same bath space but avoiding complex arithmetic altogether. While we believe that this is the most efficient way to match higher derivatives of the hybridization, in this work we only use the complex dynamic bath orbitals directly and the maximum matched derivative is simply $n = M_d - 1$.

The full frequency-dependent bath space $\mathcal{B}(z)$ is constructed as the tensor product of the individual static and dynamic bath orbitals as

$$\mathcal{B}(z) = \bigotimes_{a \in \text{imp}} \left[|b_{a,0}^{\zeta}\rangle \otimes \left(\bigotimes_{m=1}^{m \leq M_s} |b_{a,m}^{\zeta}\rangle \otimes \bigotimes_{m=1}^{m \leq M_d} |f_{a,m}^{\zeta}(z)\rangle \right) \right], \quad (16)$$

where M_s (M_d) denotes the maximum order of static (dynamic) bath orbitals. We note that the orbitals in Eqs. (12-15) are not a convenient basis for \mathcal{B} , as they are not generally orthonormal. We thus perform a QR decomposition on the matrix representing \mathcal{B} in order to obtain an orthonormalized set of bath orbitals.

While the inclusion of the first-order ($m = 1$) dynamic bath orbitals guarantees an exact matching of the hybridization, we want to emphasize that this does not completely remove the bath discretization error. To understand this, it is useful to add a parameterization in terms of an additional frequency z' to Eq. (9):

$$\Delta_c(z; z') = \sum_p \frac{N_b \Gamma_p(z') \otimes \Gamma_p^*(z')}{z - \varepsilon_p(z')}. \quad (17)$$

What we mean with *exact matching of the hybridization* is that the bath parameterization at z' guarantees that the hybridization is exact at $z = z'$, but not at other frequencies $z \neq z'$. Similarly, the higher order dynamic bath orbitals guarantee that the first, second, etc derivatives with respect to z are exact at z' . This is illustrated in Fig. 2, where the relative error of the cluster hybridization $\Delta_c(i\omega_n; i\omega_{n'})$ is plotted as a function of $i\omega_n$ for the two sets of bath orbitals parameterized for the fixed frequency points $n' = 5$ (middle panel) and $n' = 20$ (bottom panel). This is compared to the performance of the expansion in higher order *static* bath orbitals of EwDMET (top panel). While the static bath orbitals quickly reduce the hybridization error in the high frequency regime, the error at low frequencies reduces only slowly with M_s . On the other hand, the dynamic bath orbitals lead to an exact matching of the hybridization at the point they are meant to represent, while the higher order dynamic bath orbitals also construct an increasingly good match of the hybridization around these points.

Why is it important to match the hybridization at frequencies other than the frequency which is explicitly being solved

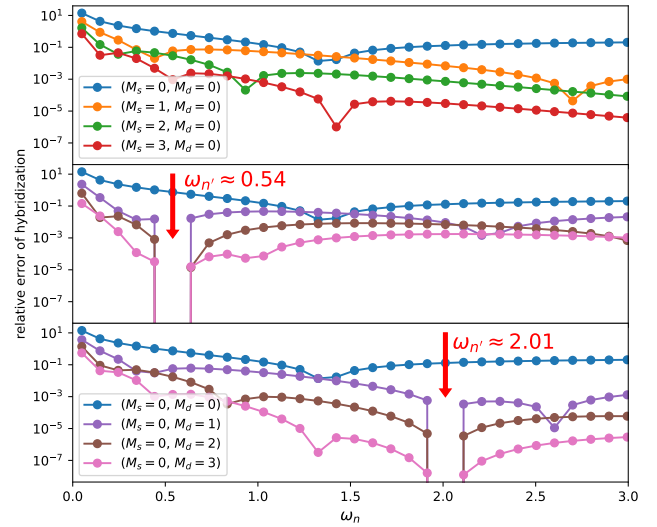


FIG. 2. Relative error of hybridization function, defined as $(\Delta_c(i\omega_n) - \Delta(i\omega_n)) / \Delta(i\omega_n)$, for the Hubbard model on the Bethe lattice at $U = 4$. The maximum order of static bath orbitals is denoted M_s and the maximum order of dynamic bath orbitals M_d . Top panel: Convergence with respect to M_s without any dynamic bath orbitals. Middle panel: The dynamic bath orbitals are evaluated at the 6th Matsubara frequency (red arrow), and the hybridization is matched exactly at this frequency. Bottom panel: The same as the middle panel, but with the dynamic bath orbitals evaluated at the 21st Matsubara frequency. It is clear that matching higher-order derivatives of the hybridization by increasing M_d at a given frequency point also improves the hybridization error away from the frequency of interest.

for with the given bath orbitals? This is because the introduction of the explicit two-particle impurity terms in the impurity model couples the hybridization at different frequency points. It is a reasonable assumption that the main relevant energy scale will be centered around the frequency point of interest, and therefore, matching the higher-order derivatives of the hybridization at the frequency point of interest seems a reasonable strategy, and one which is borne out from numerical results. Therefore, in this work we will not consider higher order static bath orbitals and always choose $M_s = 0$, and choose to systematically expand the bath space in the presence of explicit interactions by increasing the maximum dynamic bath orbital order. This simplifies Eq. (16) to

$$\mathcal{B}(z) = \bigotimes_{a \in \text{imp}} \left[|b_{a,0}^{\zeta}\rangle \otimes \left(\bigotimes_{m=1}^{m \leq M_d} |f_{a,m}^{\zeta}(z)\rangle \right) \right] \quad (18)$$

and reduces the number of bath orbitals to $N_b = N_{\text{imp}}(1 + 2M_d)$.

For ED solvers, this may still result in a prohibitively large number of bath orbitals for a larger number of impurity sites, even for the minimal case of $M_d = 1$. We thus also implement the following factorization of the dynamic bath orbital space: to calculate a column b of the particle Green's matrix $G_{ab}^>$, only the dynamic bath orbitals constructed from b , i.e. $|f_{b,m}^>(z)\rangle$ and $|f_{b,m}^<(z)\rangle$ are included in the bath space. This

can similarly hold for the rows a of the hole Green's function. This makes the bath space of Eq. (18) not only frequency, but also impurity-orbital dependent:

$$\mathcal{B}_b(z) = \bigotimes_{a \in \text{imp}} |b_{a,0}^>\rangle \bigotimes_{\zeta \in \{>,<\}} \bigotimes_{m=1}^{m \leq M_d} |f_{b,m}^\zeta(z)\rangle. \quad (19)$$

We call this approach ‘orbital factorization’, as it only matches the hybridization (and optionally its derivatives) for a single impurity orbital at a time. The number of bath orbitals (for any given cluster) then becomes $N_b = N_{\text{imp}} + 2M_d$, which makes the calculation of e.g. a complete d -shell feasible within ED for a $M_d = 1$ bath, resulting in 7 bath orbitals and a cluster size of 12. Note that an impurity-orbital dependent bath space could potentially lead to a breaking of the symmetry $G_{\text{imp},ab}(i\omega_n) = G_{\text{imp},ba}(i\omega_n)$ and require an additional symmetrization step. In the systems tested in this work, however, this symmetry was not broken. We note that this factorization is exact in the limit of $U = 0$, retaining the beneficial feature of an exact representation of the uncorrelated Green's function in the cluster space.

Another issue in standard DMFT is the electron filling of the cluster problem. In general, separate calculations with different fillings are necessary to determine the best choice, usually by selecting the filling which results in the lowest ground-state energy of the impurity model. This problem is not present in ω -DMFT: the zero-order static bath orbitals have a filling of $2 - \chi_\alpha$ where χ_α is the filling of the impurity orbital which they are derived from according to Eq. (12). Consequently, the impurity + zero-order static bath space can always be filled with a known, integer number of electrons. This property still holds when higher order static or dynamic bath orbitals are added, since these are always completely empty (particle orbitals) or completely filled (hole orbitals). As a result, the electron number of the cluster problem is known by construction and exactly matches the electron number of the projection of the lattice density matrix into the cluster space.

To conclude this section, it is worth making a connection between the ideas in this approach and the method of distributional exact diagonalization (DED).⁷ In DED, finite bath spaces for the impurity problem are sampled stochastically according to a probability distribution derived from the continuous hybridization, and the self-energy is obtained as a sample average. This corresponds to a neglect of a subset of the bath-bath cross correlation terms in the diagrammatic self-energy expansion. A similar effect occurs in the bath discretization choice of ω -DMFT. Here, there are a set of cluster problems, each constructed to best represent the hybridization effects with the environment at a given frequency. However, bath discretization errors can still emerge once interacting terms are included in the impurity Hamiltonian, as this can couple the hybridization at different frequency points. The final impurity self-energy is then a summation of the individual contributions, effectively neglecting some of the cross-frequency correlations in the self-energy expansion. However, this inter-frequency coupling is systematically converged via the addition of bath orbitals derived from the Schmidt decomposition

of higher-order dynamical functions.

2. Lattice self-energy

As mentioned above, many-body effects can be included in the lattice to describe the correlated changes to the one-particle environment of the impurity. This has an effect on the construction and nature of the bath states, and is described in DMFT via the self-consistent local self-energy. In ω -DMFT, we replace h , the one-particle part of the lattice Hamiltonian, with an augmented one-particle Hamiltonian h_{Weiss} , which is designed to represent the Weiss field of the impurity space, implicitly including the self-energy effects in the environment. In DMET this is attempted via a simple one-electron potential which cannot describe dynamical correlation effects, while in EwDMET and in this work, we additionally use a set of auxiliary states which are coupled to the system. The benefit of the latter method is that the auxiliary states are able to represent the poles of any arbitrary frequency-dependent self-energy. With the energies α and couplings β of the auxiliary states, the augmented Weiss-Hamiltonian is

$$h_{\text{Weiss}} = \sum_{ij \in \text{lat}} h_{ij} c_i^\dagger c_j + \sum_{F > 0} \left[\sum_{ij \in \mathcal{F}(F)} \Sigma_{ij}^\infty c_i^\dagger c_j + \sum_{r \in \mathcal{A}(F)} \alpha_r c_r^\dagger c_r + \sum_{i \in \mathcal{F}(F)} \sum_{r \in \mathcal{A}(F)} \beta_{ir} \left(c_i^\dagger c_r + \text{h.c.} \right) \right], \quad (20)$$

where F is an index that enumerates the symmetry equivalent fragments of the lattice with $F = 0$ being the impurity space and $\mathcal{F}(F)$ is the set of sites in F . This achieves the same replication of the self-energy in DMFT given by Eq. (8). $\mathcal{A}(F)$ denotes a subspace of the full auxiliary space, which contains auxiliaries only coupling to F . By virtue of the DMFT approximation (i.e. an impurity-local effective self-energy), no auxiliaries that couple between fragments are needed in Eq. (20). Additionally, the impurity space is excluded from the summation in Eq. (20), which is in contrast to DMET, where the correlation potential (taking the role of the static self-energy Σ^∞) is also included in the impurity space in the definition of the Hamiltonian to perform the Schmidt decomposition. This can be compared to DMFT, where the hybridization is also defined with respect to an uncorrelated impurity, as the self-energy is removed from the impurity in the final term in Eq. (9). Only the removal of the impurity space auxiliaries (and static self-energy) leads to a systematic convergence to the correct hybridization with higher orders of static or dynamic bath orbitals. We note here that previous (static) EwDMET work did not remove this local effective self-energy in the bath construction, and the effect of this will be investigated in future work.

To determine an appropriate set of auxiliary parameters α and β from the impurity self-energy, we minimize the distance functional

$$d = \sum_n \frac{1}{\omega_n} \text{tr} \left| \Sigma_{\text{aux}}(i\omega_n; \alpha\beta) - (\Sigma_{\text{imp}}(i\omega_n) - \Sigma_{\text{imp}}^\infty) \right|^2, \quad (21)$$

by variation of α and β in the auxiliary self-energy

$$\Sigma_{\text{aux}}(i\omega_n; \alpha\beta) = \sum_r^{N_{\text{aux}}} \frac{\beta_r \otimes \beta_r}{i\omega_n - \alpha_r}. \quad (22)$$

Note that this step is equivalent to the bath fit via minimization of Eq. (3) in DMFT. The only difference between bath states and auxiliary states is the physics they represent: the bath represents the delocalization and one-electron hybridization with the environment, whereas the auxiliaries above represent many-body correlation effects due to a self-energy within the impurity. While it seems that the bothersome non-linear fit of the bath orbitals from DMFT is just replaced with another fit of this kind in ω -DMFT, it has to be stressed that the auxiliaries are added to the mean-field Hamiltonian and not to the cluster problem. The computational complexity thus only increases as $\mathcal{O}(N_{\text{aux}}^3)$ instead of exponentially and converging the calculations with respect to the number of auxiliaries was not a problem for the systems in this paper, as the emphasis on a compact representation is not necessary. In practice we find that 20 auxiliary states per impurity orbital, initially distributed particle-hole symmetrically on a logarithmic energy grid between $-10t$ and $10t$ are sufficient. The initial elements of the coupling vectors were set to $0.01t$ or $-0.01t$, depending on to which sublattice of the bipartite lattice they couple to, respectively (for a calculation with a single impurity site, all elements were initially positive). It should be noted that while more auxiliaries can be added, the fit can become overcomplete, since it is performed on the Matsubara axis and many solutions can exist that minimize the difference function to a similar level of accuracy.⁶

3. Solving the impurity problem

To simplify the notation in the following, we introduce the index $\kappa(z)$, which enumerates the frequency-dependent impurity problems to be solved at each frequency (this index must not be confused with the fragment index F in Eq. (20), which labels the symmetry-equivalent impurity clusters in the lattice). If the impurity-orbital factorization is used, κ additionally depends on the impurity orbital. Denoting the projector into the space of κ as P_κ , we can then write down the embedded cluster Hamiltonian, equivalent to the auxiliary Anderson impurity model of DMFT, as

$$H_\kappa = P_\kappa h_{\text{Weiss}} P_\kappa + U \sum_{a \in \text{imp}} n_a^\uparrow n_a^\downarrow - \frac{U}{2} \sum_{a \in \text{imp}} \gamma_{aa} c_a^\dagger c_a, \quad (23)$$

where the last term subtracts the Hartree–Fock potential, which is already contained in h_{Weiss} (for simplicity we suppressed both the Hartree–Fock potential and the chemical potential term in Eq. (20), since they cancel exactly). We note that in the absence of particle-hole symmetry it becomes necessary to introduce an energy shift between impurity sites and bath sites in Eq. (23), which needs to be optimized to ensure the correct distribution of electrons between impurity and bath. For every cluster κ , we use exact diagonalization to

solve

$$H_\kappa |0_\kappa\rangle = E_{0;\kappa} |0_\kappa\rangle, \quad (24)$$

for the ground-state and LGMRES³⁸ to solve the particle and hole response equations

$$[i\omega_n - (H_\kappa^> - E_{0;\kappa})] |\phi_{a;\kappa}^>(i\omega_n)\rangle = c_a^\dagger |0_\kappa\rangle \quad (25)$$

$$[i\omega_n + (H_\kappa^< - E_{0;\kappa})] |\phi_{a;\kappa}^<(i\omega_n)\rangle = c_a |0_\kappa\rangle \quad (26)$$

for the correction vectors $|\phi_{a;\kappa}^>(i\omega_n)\rangle$ and $|\phi_{a;\kappa}^<(i\omega_n)\rangle$. Note that we cannot solve solely for the imaginary part of the correction vector as is usually done using the conjugate gradient method, because the Hamiltonian is complex.^{35,36} This could be circumvented in the case of including independent real and imaginary parts of the dynamic bath orbitals to ensure a real Hamiltonian. With the ground-state and both response states calculated, the impurity Green's function is simply

$$G_{\text{imp},ab}(i\omega_n) = \langle 0_\kappa | c_a | \phi_{b;\kappa}^>(i\omega_n) \rangle + \langle \phi_{a;\kappa}^<(i\omega_n) | c_b | 0_\kappa \rangle, \quad (27)$$

and the impurity self-energy is given by the Dyson equation

$$\Sigma_{\text{imp}}(i\omega_n) = P_{\text{imp}} [i\omega_n - h_{\text{Weiss}}]^{-1} P_{\text{imp}} - G_{\text{imp}}^{-1}(i\omega_n), \quad (28)$$

where P_{imp} is a projector into the impurity space. Note that in Eq. (28), we could have used the cluster projection instead of the full h_{Weiss} (i.e. $P_\kappa h_{\text{Weiss}} P_\kappa$). This is because the uncorrelated Green's function will always truthfully be represented in the cluster space due to the first-order dynamic bath orbitals. In DMFT on the other hand, these two choices differ, the first corresponding to using the true hybridization $\Delta(i\omega_n)$ for the bath Green's function in Eq. (7) and the latter to using the fitted cluster hybridization $\Delta_c(i\omega_n)$ (In practice, in DMFT $\Delta_c(i\omega_n)$ is used for a better cancellation of bath discretization error between the Weiss and impurity Green's function).

C. Self-consistent Algorithm

With the main steps of a ω -DMFT described above, we now summarize the self-consistent algorithm. The method starts from an initial guess for the impurity self-energy, which can be taken from a different method, a different model (e.g. a converged self-energy at a slightly different U value), or if no such self-energy is available, can be set to zero. The steps of the algorithm are then as follows:

1. Fit the auxiliary parameters α , β to the impurity self-energy via minimization of Eq. (21).
2. Construct and diagonalize h_{Weiss} (20) to obtain the eigenvalues ε and eigenvectors C .
3. Construct static and dynamic bath orbitals according to Eqs. (12-15). Orthonormalize the resulting bath matrix.
4. For each cluster κ , solve the ground-state equation (24) with ED and the response equations (25,26). From the ground and response states, construct the impurity Green's function (27) and the new impurity self-energy via the Dyson equation (28).

5. To improve the stability of the algorithm, we mix the old and new self-energy according to $\Sigma_{\text{imp}} = (1 - \alpha_{\text{mix}})\Sigma_{\text{imp}}^{\text{new}} + \alpha_{\text{mix}}\Sigma_{\text{imp}}^{\text{old}}$ with $\alpha_{\text{mix}} = 0.25$.

These steps are iterated, until the calculation converges. As convergence criteria, we check that

$$\left\| \Sigma_{\text{imp},ab}(\mathbf{i}\omega_n) - \Sigma_{\text{imp},ab}^{\text{old}}(\mathbf{i}\omega_n) \right\|_{\text{F}} < (1 - \alpha_{\text{mix}}) (10^{-4} + 10^{-3} \left\| \Sigma_{\text{imp},ab}(\mathbf{i}\omega_n) \right\|_{\text{F}}) \forall n, a, b, \quad (29)$$

where $\|\dots\|_{\text{F}}$ denotes the Frobenius norm.

D. Spectral function

In ED-DMFT it is possible to get the real-frequency spectrum after the bath parameters are converged on the Matsubara axis. In principle, the same approach could be used in ω -DMFT, however in contrast to DMFT, the dynamic bath orbitals in Eqs. (14,15) would change with the transformation $z = \mathbf{i}\omega_n \rightarrow \omega + \mathbf{i}\eta$. Unfortunately, performing ω -DMFT on the real axis results in little control over the sum rules in a frequency-factorized formulation (even though we find that in practice the spectra obtained in this manner are generally quite close to being normalized). We thus choose instead to calculate the spectrum from the auxiliary model of the self-energy, which must yield a causal and normalized spectral function by construction, as the self-energy is represented in the form of Eq. 22. The mean-field Hamiltonian used for this is

$$h_{\text{aux}} = \sum_{ij \in \text{lat}} h_{ij} c_i^\dagger c_j + \sum_{F=0} \left[\sum_{ij \in \mathcal{F}(F)} \Sigma_{ij}^\infty c_i^\dagger c_j + \sum_{r \in \mathcal{A}(F)} \alpha_r c_r^\dagger c_r + \sum_{i \in \mathcal{F}(F)} \sum_{r \in \mathcal{A}(F)} \beta_{ir} (c_i^\dagger c_r + \text{h.c.}) \right], \quad (30)$$

which differs from the Weiss Hamiltonian (20) only by inclusion of the auxiliaries coupling to the impurity, i.e. the summation over F includes $F = 0$, as the implicit self-energy is now included in the impurity space. The impurity part of the spectral function is then simply given by

$$A(\omega) = -\frac{1}{\pi} \text{Im} P_{\text{imp}} \frac{1}{\omega - h_{\text{aux}} + \mathbf{i}\eta} P_{\text{imp}}. \quad (31)$$

Note that this is equivalent to calculating the spectral function in the lattice space in DMFT according to Eq. (10).

1. Total energy

The total energy per site of the DMFT and ω -DMFT method can be calculated according to the Galitskii-Migdal

equation³⁹

$$E = \frac{1}{N_{\text{imp}}} \left[\sum_{a \in \text{imp}} \sum_{i \in \text{lat}} \left(h_{ai} + \delta_{ia} \frac{\gamma_{aa} U}{4} \right) \gamma_{ia} + \sum_{ab \in \text{imp}} \int_{-\infty}^{\infty} G_{ab}(\mathbf{i}\omega_n) \Sigma_{ba}^{\text{dyn}}(\mathbf{i}\omega_n) d\omega \right], \quad (32)$$

where $\Sigma^{\text{dyn}}(\mathbf{i}\omega_n)$ is the dynamic part of the lattice self-energy and h , γ , and $G(\mathbf{i}\omega_n)$, are the lattice Hamiltonian, density-matrix, and Green's function. The first term corresponds to the static Hartree-Fock-like contribution and the second term takes dynamic self-energy contributions into account. If the electron correlation does not lead to a breaking of the occupation symmetry, i.e. the diagonal of the correlated density matrix γ_{aa} is constant, the first term becomes identical to the Hartree-Fock energy and the second one becomes the correlation energy of the method. By calculating the energy in the lattice space, instead of the cluster space, the explicit dependence of the energy on the bath discretization is removed in both methods. However, an implicit dependence on the bath discretization error remains via the self-consistent density matrix, Green's function, and self-energy.

III. RESULTS

We test the ω -DMFT method using the Hubbard model on an infinite-dimensional Bethe lattice, a 1D chain, and a 2D square lattice. For all calculations, we use 800 Matsubara points and a fictitious temperature of $T = 0.01$. We note that this does not correspond to a finite temperature calculation, but rather a choice of Matsubara discretization since the impurity problem is being solved for the ground-state only.

A. The Hubbard model on the infinite-dimensional Bethe lattice

The Hubbard model in infinite dimensions is an ideal benchmark for quantum embedding methods, since the self-energy is purely local and the DMFT approximation becomes exact.⁴⁰ In this model, it is found that at a critical value of U there exists a metal to Mott insulator quantum phase transition, with $U_C = 5.88$. We model the Bethe lattice density of states (DoS) via 200 particle-hole symmetric states, fitted to produce a semi-circular DoS, with every state being subject to the Hubbard- U interaction.⁴¹ In Fig. 3 the convergence of the impurity self-energy with respect to the dynamic bath order M_d is compared to a DMFT calculation with 7 bath orbitals ($M_d = 1$ has 3 bath orbitals, $M_d = 2$ has 5, and $M_d = 3$ has 7), showing both the converged self-energy, and the difference to DMFT with 7 bath orbitals. The calculations were started from a self-energy converged at a slightly higher value of U , when available. At low U ω -DMFT self-energies are in excellent agreement with DMFT, even when a smaller number of bath orbitals is used. Just before the Mott-insulator-transition (MIT) at $U = 5$ more dynamic bath orders are

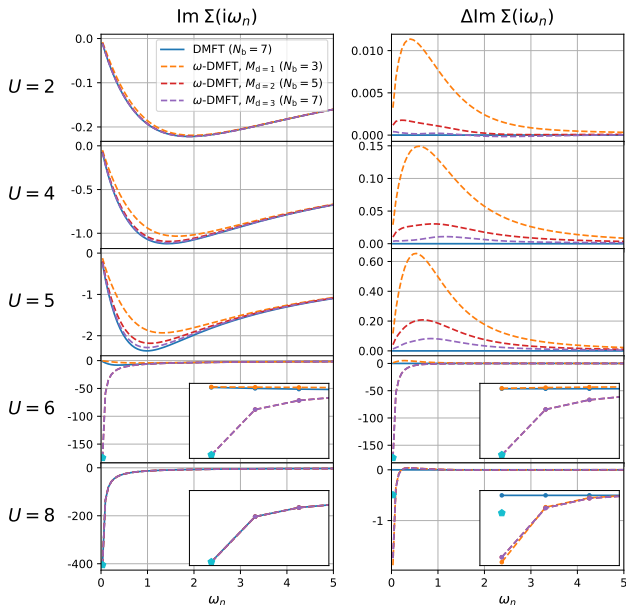


FIG. 3. Left column: Imaginary part of converged Matsubara self-energy for the infinite-dimensional Bethe lattice Hubbard model. The number in parenthesis indicates the number of bath orbitals. Right column: Difference of the self-energy with respect to DMFT ($N_b = 7$). For $U = 6$ and $U = 8$, the inset shows the first three Matsubara points to focus on the low-energy regime, with the pentagon denoting the first Matsubara point of a DMFT calculation with 9 bath orbitals to compare the convergence.

needed to recover the DMFT self-energy. At $U = 6$, DMFT with 7 bath orbitals and the ω -DMFT calculation with $M_d = 1$ favor the metallic solution favoured at lower U , whereas ω -DMFT with $M_d = 2$ and $M_d = 3$ transition to the insulating solution. The insulating solution at $U = 6$ is in agreement with the critical value of $U_C = 5.88$ reported in Ref. 42 using the numerical renormalization group method, indicating that the ω -DMFT with $M_d = 2$ and 3 are more accurate than the corresponding DMFT calculation with 7 bath orbitals. To corroborate this, we have also performed DMFT with 9 fitted bath orbitals, and find that the solution becomes insulating with this enlarged bath space, demonstrating the accuracy and compact nature of the bath space for ω -DMFT. In both the insulating solutions at $U = 6$ and 8, the converged self-energy for $M_d = 2$ and 3 are close to identical, indicating that ω -DMFT is well converged with respect to the bath size, while even at $U = 8$, there still remain large differences seen in moving from 7 to 9 fit bath orbitals. Overall, for this model, the ω -DMFT self-energy appears well converged with $M_d = 2$, resulting in 5 bath orbitals, whereas DMFT with 7 bath orbitals still has not converged with respect to bath size, evidenced most clearly by the qualitatively incorrect solution at $U = 6$, as is apparent by comparison to DMFT with $N_b = 9$. This demonstrates the compact nature of the ω -DMFT bath space.

Figure 4 shows the local DoS resulting from the converged self-energy from ω -DMFT using $M_d = 3$ in comparison to

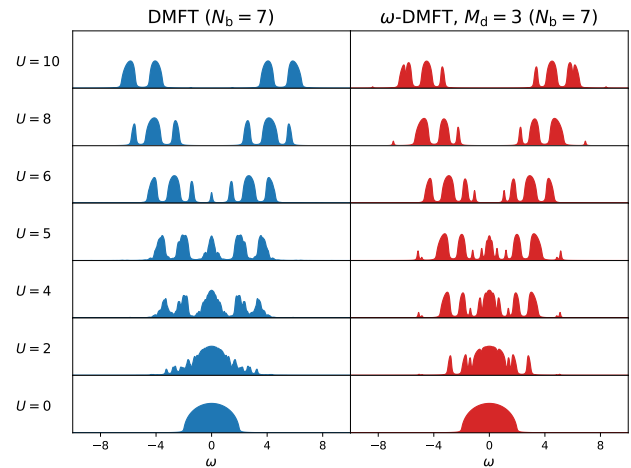


FIG. 4. Impurity DoS of the infinite-dimensional Hubbard model on the Bethe lattice for DMFT with 7 bath orbitals, and ω -DMFT with $M_d = 3$. While the transition to an insulating state is made by $U = 6$ within ω -DMFT, the DMFT solution is still erroneously metallic. A Lorentzian broadening of $\eta = 0.05$ was used for both.

DMFT with 7 bath orbitals. The spectra are in broad agreement for all values of U , while at $U = 6$ the DMFT solution still has a small quasiparticle peak, whereas the ω -DMFT solution is fully insulating. The ω -DMFT spectral functions can also show more high-energy features than DMFT, although it is not clear if these are physical, or a result of the auxiliary representation of the self-energy.

B. The 1D Hubbard model

The 1D Hubbard chain is a difficult system for single-site DMFT, since both short and long-range correlation are important, and the DMFT approximation is far from its exact infinite-dimensional limit. Here we consider an impurity cluster of 2 sites, so that nearest neighbor correlations can be captured explicitly within the impurity model. This cluster also allows for assessment of the accuracy of the impurity-orbital factorization of the bath space. The full lattice consists of 400 sites with anti-periodic boundary conditions, so that finite-size effects of the lattice become negligible. Figure 5 compares the trace of the Matsubara self-energies obtained with DMFT ($N_b = 6$) and ω -DMFT using $M_d = 1$, which results in 2 static and 4 dynamic bath orbitals. Additionally, we also test the orbital factorization (denoted $M_d = 1^*$) of the dynamic bath space according to Eq. (19), which leads to only 2 static and 2 dynamic bath orbitals. Evidently, the 1D Hubbard model requires a smaller number of bath orbitals for a good description of the hybridization than the (formally) infinitely coordinated Bethe lattice, which can be argued on simple quantum information grounds. The self-energies of all three methods are very similar, with only very minor discrepancies between the methods at all U , where it is unclear which method is more accurate. The orbital factorization addition-

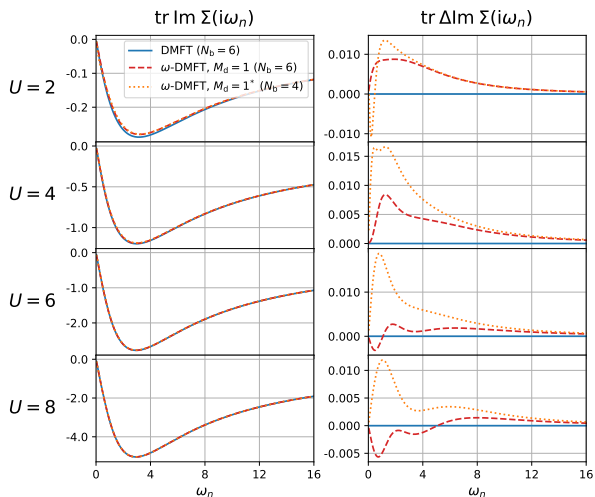


FIG. 5. Similar to Fig. 3 but for the 1D Hubbard model with a 2-site impurity. The trace of the self-energy is shown. Discrepancies between DMFT and ω -DMFT are exceptionally small across all correlation regimes, even utilizing the additional orbital factorization approximation.

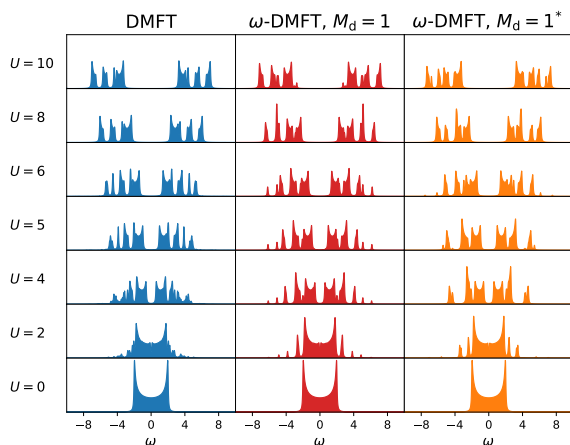


FIG. 6. Trace of the local DoS of the 1D Hubbard model with a 2-site impurity. A broadening of $\eta = 0.05$ was used.

ally only leads to very small changes in the self-energy. Note that although Fig. 5 only shows the trace of the self-energy, it will still be affected by any errors in the off-diagonal parts of the impurity Green's function resulting from the orbital factorization, due to the inversion of the Green's function in the Dyson equation. In Figure 6, the spectral functions of the three different methods are shown. Again, DMFT and ω -DMFT spectral functions are almost identical, especially in the low frequency regime. Finally, in Fig. 7, we compare the total energy per site of DMFT and ω -DMFT to the exact thermodynamic limit energy obtained from the Bethe ansatz.⁴³ To illustrate the strength of the electron correlation at different values of U , we also show the restricted Hartree-Fock (RHF) energy. All energy curves lie on top of each other and are

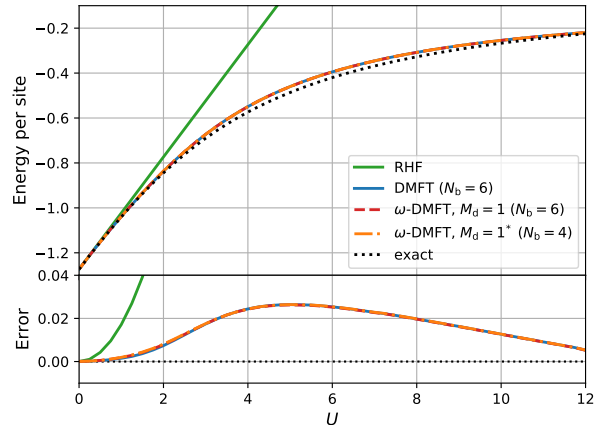


FIG. 7. Top row: Ground-state energy per site of the 1D Hubbard model, calculated according to Eq. (32). Bottom row: Error in the total energy, compared to the exact solution from the Bethe ansatz.

very close to the exact energy at low and high values of U . In the intermediate region, both DMFT and ω -DMFT underestimate the total energy, due to the neglect of long-range correlation. In conclusion, both the standard ω -DMFT and the orbital-factorized variation agree with the results of DMFT for the two-impurity 1D Hubbard model without appreciable error.

C. The 2D Hubbard model

The 2D Hubbard model on a square lattice is a challenging system for embedding methods. On the one hand, the dimensionality is not high enough to make single-site DMFT accurate, as it is in the case of the Bethe lattice. On the other hand, more bath states are needed to describe the hybridization than in the one-dimensional case, severely restricting either the impurity size or the bath size of cluster DMFT calculations. Although the true ground-state is expected to be gapped at any finite- U value, for finite clusters embedded in a paramagnetic phase, the absence of fixed (static) magnetic moments developing in the environment constrains the description of the long-range spin fluctuations, and precludes the opening of a gap at low U ⁴⁴. Therefore, when restricted to paramagnetic phases, the model develops a finite- U phase transition from metallic to Mott-insulating state, which is used as an example of the physical processes governing this correlation-driven behavior present in many two-dimensional systems. This universal behavior is also seen in the restriction of QMC wavefunction ansatz to paramagnetic forms.⁴⁵

Here we consider square fragments of 2×2 sites on a lattice of size 48×24 with anti-periodic boundary conditions in both dimensions. An additional difficulty in standard ED-DMFT calculations is that the lattice geometry can put constraints on the bath parameterization. These can be taken into account, but this requires knowledge about the system at hand and re-

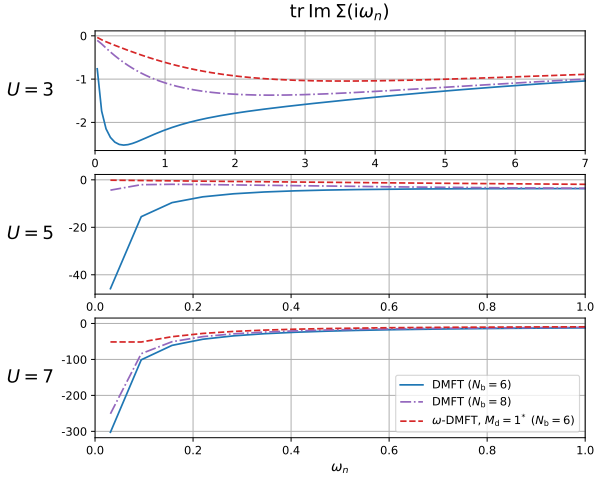


FIG. 8. Trace of the imaginary part of the impurity Matsubara self-energy of the 2D Hubbard lattice for three representative correlation strengths, for DMFT with $N_b = 6$ and 8 orbitals, and ω -DMFT with 6 bath orbitals. Note the different scales of the frequency axes, allowing a clearer resolution of the differences in the low energy regime for higher U .

duces the functional space onto which the hybridization is projected. We chose to not apply any symmetry constraints to the bath parameters, except for those due to particle-hole symmetry as mentioned in Sec. III B. For the ω -DMFT method, we applied the orbital factorization (denoted $M_d = 1^*$), resulting in 6 bath orbitals.

Figure 8 compares the trace of the imaginary part of the impurity self-energy of DMFT with 6 bath orbitals, 8 bath orbitals, and ω -DMFT (6 bath orbitals). At $U = 3$, ω -DMFT underestimates the self-energy in comparison to DMFT ($N_b = 8$), but yields a self-energy that is closer to DMFT ($N_b = 8$) than a DMFT calculation with only 6 bath orbitals, which substantially overestimates the correlation. This manifests in the spectrum (Fig. 9) as an erroneous removal of the sharp quasi-particle peak derived from the van Hove singularity at $\omega = 0$ for DMFT ($N_b = 6$), which is retained in both the 8 bath orbital results, and the ω -DMFT approach demonstrating the compactness of this bath space. The behavior is exacerbated at $U = 5$, where DMFT with 6 bath orbitals clearly has an insulating solution, with distinct spectral gap and a divergent self-energy. Increasing this to 8 bath orbitals changes the character to mostly metallic, except for the first Matsubara point which indicates a potential divergence, but a spectrum which looks metallic. In contrast, the ω -DMFT self-energy is entirely metallic and much closer to the DMFT ($N_b = 8$) result than DMFT ($N_b = 6$). The spectrum of Fig. 9 at this U value retains the sharp feature at the Fermi level, with a similar height as the ones for lower values of U (and thus fulfilling the Luttinger theorem). The higher frequency part of the self-energy then serves to develop significant Hubbard side-bands in the spectrum. This character is anticipated and follows the trend of increasing numbers of bath orbitals in DMFT, as well as the comparable literature DMFT suggesting a metallic solution at this U ⁴⁶. At $U = 7$ and $U = 9$, ω -DMFT again has a

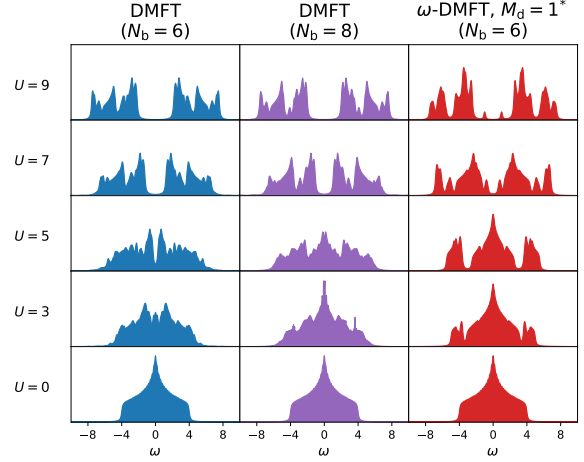


FIG. 9. Trace of the impurity-projected lattice DoS for the 2D Hubbard model. The calculations were converged on a 48×24 lattice and the resulting self-energy (DMFT) or auxiliaries (ω -DMFT) were put on a 60×60 lattice, to obtain smoother spectra. A broadening of $\eta = 0.1$ was used.

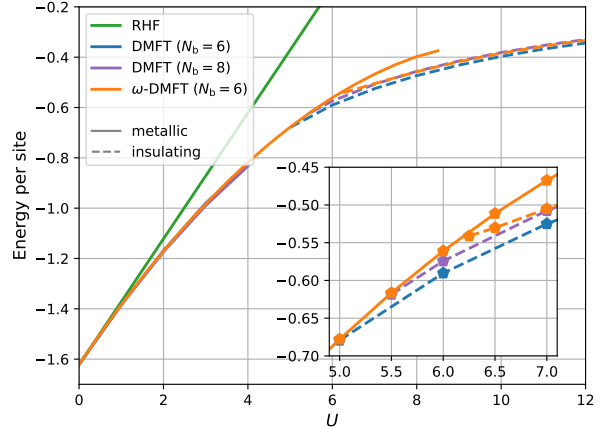


FIG. 10. Energy per site of the 2D Hubbard model, calculated according to Eq. (32), for DMFT with $N_b = 6$ and 8 orbitals, and ω -DMFT with 6 bath orbitals. Metallic solutions are given by solid lines, while the insulating solutions are dashed. The inset shows a zoom of the transition region, showing the slightly higher U metal-insulator transition for the ω -DMFT than DMFT, although the larger number of bath orbitals tends towards this value.

smaller value of the self-energy in the low-frequency regime than both DMFT self-energies, resulting in a slightly smaller gap, with additional small low-energy features. However all approaches result in a gapped solution. We note, however, that at all values of U the DMFT self-energy becomes more similar to the ω -DMFT self-energy as the number of bath orbitals is increased.

Finally, Fig. 10 shows the total energy per site. In the metallic regime below the Mott transition, the energies of DMFT and ω -DMFT are almost identical. Above the transition, the

ω -DMFT energy is close to the DMFT curve obtained with 8 bath orbitals, while DMFT with 6 bath orbitals underestimates the energy by approximately $0.015t$. The MIT occurs between $U = 6$ and $U = 6.25$ in ω -DMFT and no metastable insulating phase was found for $U < U_C$. On the other hand, the metallic ω -DMFT solution is metastable up to $U_{C_2} = 8.5$. The slope of the total energies changes discontinuously between metallic and insulating solution at U_C (see inset of Fig. 10), which indicates a first-order phase transition. In our DMFT calculation with 8 bath orbitals, the insulating solution is stable down to $U = 5.5$ and no discontinuity of the derivative of the energy is visible.

The non-existence of a metastable insulating phase below U_C is in agreement with the cluster DMFT results from Ref. 46, which also suggest that the zero-temperature transition U_C coincides with the lower second order critical point U_{C_1} . However, the values of the critical points reported in Ref. 46 are lower ($U_{C_1} \approx 5.8$ and $U_{C_2} \approx 6.25$). These discrepancies could be due to the finite-temperature extrapolation of this work, or the remaining bath discretization error in the ω -DMFT.

IV. CONCLUSION

We have shown a way to algebraically construct frequency-dependent bath orbitals, which are designed to exactly reproduce the hybridization of the impurity to its environment, and be systematically expandable in the presence of interactions. These dynamic bath orbitals can be used in the self-consistent ω -DMFT method presented here, avoiding the difficult non-linear fit required in most ED-DMFT formulations. We show that ω -DMFT can reproduce the self-energies, density-of-states, and total energies of DMFT calculations for the Hubbard model on the infinitely coordinated Bethe lattice and the two-impurity 1D chain across all correlation strengths. In the case of the Bethe lattice, ω -DMFT correctly places the Mott-Insulator transition between $U = 5$ and $U = 6$ with only 5 bath orbitals. On the other hand, in standard ED-DMFT 9 bath orbitals are needed to place the transition in this interval, with fewer bath orbitals resulting in too high a transition between $U = 6$ and $U = 7$. We also applied ω -DMFT to the 2D square lattice with a 2×2 impurity cluster, employing an orbital factorization to obtain a manageable bath size of only 6 orbitals. In the metallic regime the self-energies of ω -DMFT were shown to be in better agreement with DMFT results with 8 bath orbitals, than a DMFT calculation with 6 bath orbitals. In the insulating regime, ω -DMFT self-energies and density-of-states differ from the DMFT results at low frequency, although the latter tend towards ω -DMFT with increasing bath size. The total energy of ω -DMFT is in good agreement with DMFT with 8 bath orbitals, with the first-order phase transition predicted to be between $U = 6$ and $U = 6.25$ and thus slightly higher than in DMFT with a finite-temperature CT-QMC solver ($U_C \approx 5.8$ in Ref. 46).

The weight of numerical evidence across these different systems indicates that the frequency-dependent bath of ω -DMFT can allow for a more compact representation of the

hybridization, allowing for a more faithful representation of the impurity problem, leading to excellent results, with lower computational resources. In the future, we hope to combine this approach with emerging approximate Hamiltonian impurity solvers, which will allow the application to larger impurity spaces, and a rigorous expansion of the dynamic bath space in ω -DMFT. This will allow application to systems with long-range interactions, including moving towards *ab initio* correlated materials. Furthermore, for solvers which would not work well computing the Green's function at individual frequency points (e.g. imaginary-time solvers), the method can be recast to analytically compute *time-dependent* bath orbitals in a systematic fashion, which will be investigated in the future.

V. ACKNOWLEDGEMENTS

G.H.B. gratefully acknowledges support from the Royal Society via a University Research Fellowship, in addition to funding from the European Union's Horizon 2020 research and innovation programme under grant agreement No. 759063. We are also grateful to the UK Materials and Molecular Modelling Hub for computational resources, which is partially funded by EPSRC (EP/P020194/1).

- ¹E. Morosan, D. Natelson, A. H. Nevidomskyy, and Q. Si, *Adv. Mater.* **24**, 4896 (2012).
- ²W. Metzner and D. Vollhardt, *Phys. Rev. Lett.* **62**, 324 (1989).
- ³X. Y. Zhang, M. J. Rozenberg, and G. Kotliar, *Phys. Rev. Lett.* **70**, 1666 (1993).
- ⁴A. Georges, G. Kotliar, W. Krauth, and M. J. Rozenberg, *Rev. Mod. Phys.* **68**, 13 (1996).
- ⁵E. Gull, A. J. Millis, A. I. Lichtenstein, A. N. Rubtsov, M. Troyer, and P. Werner, *Rev. Mod. Phys.* **83**, 349 (2011).
- ⁶Y. Lu and M. W. Haverkort, *Eur. Phys. J. Spec. Top.* **226**, 2549 (2017).
- ⁷M. Granath and H. U. R. Strand, *Phys. Rev. B* **86**, 115111 (2012).
- ⁸D. Zgid, E. Gull, and G. K.-L. Chan, *Phys. Rev. B* **86**, 165128 (2012).
- ⁹A. Go and A. J. Millis, *Phys. Rev. B* **96**, 085139 (2017).
- ¹⁰F. Mejtuto-Zaera, N. M. Tubman, and K. B. Whaley, (2019), arXiv:1711.04771.
- ¹¹F. A. Wolf, A. Go, I. P. McCulloch, A. J. Millis, and U. Schollwöck, *Phys. Rev. X* **5**, 041032 (2015).
- ¹²M. Ganahl, M. Aichhorn, H. G. Evertz, P. Thunström, K. Held, and F. Verstraete, *Phys. Rev. B* **92**, 155132 (2015).
- ¹³F. A. Wolf, J. A. Justiniano, I. P. McCulloch, and U. Schollwöck, *Phys. Rev. B* **91**, 115144 (2015).
- ¹⁴T. Zhu, C. A. Jimenez-Hoyos, J. McClain, T. C. Berkelbach, and G. K.-L. Chan, (2019), arXiv:1905.12050.
- ¹⁵A. Shee and D. Zgid, (2019), arXiv:1906.04079.
- ¹⁶E. Sheridan, C. Weber, E. Plekhanov, and C. Rhodes, *Phys. Rev. B* **99**, 205156 (2019).
- ¹⁷N. S. Blunt, A. Alavi, and G. H. Booth, *Phys. Rev. Lett.* **115**, 050603 (2015).
- ¹⁸G. H. Booth and G. K.-L. Chan, *J. Chem. Phys.* **137**, 191102 (2012).
- ¹⁹K. Guthrie, W. Dobrutz, O. Gunnarsson, and A. Alavi, *Phys. Rev. Lett.* **121** (2017).
- ²⁰G. Knizia and G. K.-L. Chan, *Phys. Rev. Lett.* **109**, 186404 (2012).
- ²¹B.-X. Zheng and G. K.-L. Chan, *Phys. Rev. B* **93**, 035126 (2016).
- ²²B.-X. Zheng, C.-M. Chung, P. Corboz, G. Ehlers, M.-P. Qin, R. M. Noack, H. Shi, S. R. White, S. Zhang, and G. K.-L. Chan, *Science* **358**, 1155 (2017).
- ²³G. H. Booth and G. K.-L. Chan, *Phys. Rev. B* **91**, 155107 (2015).
- ²⁴E. Fertitta and G. H. Booth, *Phys. Rev. B* **98**, 235132 (2018).
- ²⁵E. Fertitta and G. H. Booth, *J. Chem. Phys.* **151**, 014115 (2019).

- ²⁶S. Wouters, C. A. Jiménez-Hoyos, and G. K.L. Chan, in *Fragmentation* (John Wiley & Sons, Ltd, Chichester, UK, 2017) pp. 227–243.
- ²⁷K. Balzer and M. Eckstein, *Phys. Rev. B* **89**, 035148 (2014).
- ²⁸G. Kotliar, S. Y. Savrasov, K. Haule, V. S. Oudovenko, O. Parcollet, and C. A. Marianetti, *Rev. Mod. Phys.* **78**, 865 (2006).
- ²⁹A. Liebsch and H. Ishida, *J. Phys. Condens. Matter* **24**, 053201 (2012).
- ³⁰R. Bulla, T. A. Costi, and T. Pruschke, *Rev. Mod. Phys.* **80**, 395 (2008).
- ³¹R. Peters, T. Pruschke, and F. B. Anders, *Phys. Rev. B* **74**, 245114 (2006).
- ³²Q. Si, M. J. Rozenberg, G. Kotliar, and A. E. Ruckenstein, *Phys. Rev. Lett.* **72**, 2761 (1994).
- ³³C. Mejuto-Zaera, L. Zepeda-Núñez, M. Lindsey, N. Tubman, K. B. Whaley, and L. Lin, (2019), arXiv:1907.07191.
- ³⁴P. Prelovšek and J. Bonča, “Ground state and finite temperature lanczos methods,” in *Strongly Correlated Systems: Numerical Methods*, edited by A. Avella and F. Mancini (Springer Berlin Heidelberg, Berlin, Heidelberg, 2013) pp. 1–30.
- ³⁵Z. G. Soos and S. Ramasesha, *J. Chem. Phys.* **90**, 1067 (1989).
- ³⁶T. D. Kühner and S. R. White, *Phys. Rev. B* **60**, 335 (1999).
- ³⁷S. Wouters, C. A. Jiménez-Hoyos, Q. Sun, and G. K.-L. Chan, *J. Chem. Theory Comput.* **12**, 2706 (2016).
- ³⁸A. H. Baker, E. R. Jessup, and T. Manteuffel, *SIAM J. Matrix Anal. Appl.* **26**, 962 (2005).
- ³⁹M. V. Galitskii and A. B. Migdal, *Sov. Phys. JETP* **7**, 96 (1958).
- ⁴⁰A. Georges and G. Kotliar, *Phys. Rev. B* **45**, 6479 (1992).
- ⁴¹M. Kollar, *Int. J. Mod. Phys. B* **16**, 3491 (2002).
- ⁴²R. Bulla, *Phys. Rev. Lett.* **83**, 136 (1999).
- ⁴³E. H. Lieb and F. Y. Wu, *Phys. Rev. Lett.* **20**, 1445 (1968).
- ⁴⁴T. Schäfer, F. Geles, D. Rost, G. Rohringer, E. Arrigoni, K. Held, N. Blümer, M. Aichhorn, and A. Toschi, *Phys. Rev. B* **91**, 125109 (2015).
- ⁴⁵L. F. Tocchio, F. Becca, and C. Gros, *Phys. Rev. B* **83**, 195138 (2011).
- ⁴⁶H. Park, K. Haule, and G. Kotliar, *Phys. Rev. Lett.* **101**, 186403 (2008).